Analytical and Bioanalytical Chemistry (2021) 413:3749–3761
https://doi.org/10.1007/s00216-021-03323-6

RESEARCH PAPER

Characterization and purification of pentameric chimeric protein particles using asymmetric flow field-flow fractionation coupled with multiple detectors

Jan Kotoucek[1] · Renata Hezova[1] · Alena Vrablikova[1] · Frantisek Hubatka[2] · Pavel Kulich[1] · Stuart Macaulay[3] · Dierk Roessner[4] · Milan Raska[5] · Ivan Psikal[1] · Jaroslav Turanek[2,5,6,7]

Received: 25 January 2021 / Revised: 10 March 2021 / Accepted: 31 March 2021 / Published online: 10 April 2021

Abstract

Porcine circovirus causes the post-weaning multi-systemic wasting syndrome. Despite the existence of commercial vaccines, the development of more effective and cheaper vaccines is expected. The usage of chimeric antigens allows serological differentiation between naturally infected and vaccinated animals. In this work, recombinant pentameric vaccination protein particles spontaneously assembled from identical subunits-chimeric fusion proteins derived from circovirus capsid antigen Cap and a multimerizing subunit of mouse polyomavirus capsid protein VP1 were purified and characterized using asymmetric flow field-flow fractionation (AF4) coupled with UV and MALS/DLS (multi-angle light scattering/dynamic light scattering) detectors. Various elution profiles were tested, including constant cross-flow and decreasing cross-flow (linearly and exponentially). The optimal sample retention, separation efficiency, and resolution were assessed by the comparison of the hydrodynamic radius (R_h) measured by online DLS with the R_h values calculated from the simplified retention equation according to the AF4 theory. The results show that the use of the combined elution profiles (exponential and constant cross-flow rates) reduces the time of the separation, prevents undesirable sample-membrane interaction, and yields better resolution. Besides, the results show no self-associations of the individual pentameric particles into larger clusters and no sample degradation during the AF4 separation. The R_g/R_h ratios for different fractions are in good correlation with morphological analyses performed by transmission electron microscopy (TEM). Additionally to the online analysis, the individual fractions were subjected to offline analysis, including batch DLS, TEM, and SDS-PAGE, followed by Western blot.

Keywords Circovirus · Recombinant antigen · Asymmetric flow field-flow fractionation (AF4)

Introduction

Porcine circovirus (PCV) is one of the smallest animal viruses belonging to the genus *Circovirus*, family *Circoviridae*, and consists of a circular, single-stranded DNA with 1.7–2 kb in size. PCV virion is a nonenveloped, icosahedral particle of approximately 20 nm in diameter [1, 2]. PCV2 is considered an infectious agent that causes several porcine circovirus-associated diseases (PCVAD). The clinical manifestation of PCVAD, post-weaning multi-systemic wasting syndrome

✉ Jaroslav Turanek
turanek@seznam.cz; jaroslav.turanek@nexars.com

[1] Veterinary Research Institute, Hudcova 70, 621 00 Brno, Czech Republic

[2] C2P s.r.o. (NEXARS), The Campus Science Park, Palachovo náměstí 726/2, 625 00 Brno, Czech Republic

[3] Malvern Panalytical Ltd., Enigma Business Park, Grovewood Road, Great Malvern WR14 1XZ, UK

[4] Wyatt Technology Europe GmbH, Hochstraße 12a, 56307 Dernbach, Germany

[5] Department of Immunology, Faculty of Medicine and Dentistry, Palacky University Olomouc, Hnevotínska 3, 775 15 Olomouc, Czech Republic

[6] Inst Clin Immunol & Allergol, Charles University Prague, Univ Hosp Hradec Kralove, Sokolská 581, 50005 Hradec Kralove, Czech Republic

[7] Institute of Physics AS, Na Slovance 1999/2, 182 00 Prague 8, Czech Republic

(PMWS) [3], is characterized by chronic wasting and severely impaired weight gain in piglets 6 to 11 weeks old. This disease has had a significant economic impact on pork industries worldwide [4]. Vaccination is the most effective strategy to decrease the mortality rate and improve the growth in PCVAD-affected pig populations under field conditions [5]. Commercial PCV2 vaccines can be subdivided into three types, commonly referred to as inactivated vaccine, chimeric virus vaccine, and subunit vaccine. The present subunit vaccines (Ingelvac CircoFLEX, Boehringer Ingelheim Vetmedica), Circumvent (Intervet/Merck), and Porcilis PCV (Schering-Plow/Merck) are based on the capsid (Cap) protein of PCV2 produced in a baculovirus expression system (BEVS). For Porcilis PCV, a portion of the Cap protein is reported to be in the form of virus-like particles (VLPs) [6, 7].

Despite the existence of commercial vaccines, there is still a strong effort to develop other effective vaccines for animal use that would be cheaper with the same or better efficacy. Significant commercial potential exists for BEVS technology to produce very rapidly large quantities of various proteins including chimeric proteins such as here reported PCV2b Cap. This protein is fused with the C-terminus of the mouse polyomavirus (MPyV) capsid protein VP1 which forms a pentamer chimeric protein VP1-Cap allowing serological differentiation between infected (only Cap-reacting) and vaccinated (both VP1- and Cap-reacting) animals.

Based on the previous study of Fraiberk M. et al. [8], we produced, purified, and characterized chimeric pentamers of the mouse polyomavirus VP1 capsid protein carrying covalently bound porcine circovirus 2 capsid molecules (PCV2b Cap), VP1-Cap. The specific expression does not allow the formation of VLPs [8]. Purification and complex characterization of antigens are the crucial steps in vaccine development and industrial production. A variety of analytical techniques can be used to characterize and purify proteins/protein particles, such as size exclusion chromatography, electrophoresis, or ultracentrifugation. Concerning large recombinant antigen complexes like VLPs or multimeric protein antigens, these techniques could have limitations, including low selectivity, modification, or aggregation of the sample during analysis and low sample recovery due to the interaction of the sample with the stationary phases. The field-flow fractionation (FFF) separation technique is complementary to the above techniques [9]. The instrumentally most developed FFF sub-technique is the asymmetric flow field-flow fractionation (AF4) [10–13] which is used in a wide range of biological applications, including the study of polymers [11, 14], colloidal particles [15–17], viruses [18, 19], virus-like particles [20, 21], and proteins [20, 22, 23].

The asymmetric flow field-flow fractionation is based on a different displacement of the sample in an empty trapezoidal channel. The method uses two flows: *detector (axial) flow*, with a parabolic flow profile along the channel axis, and the *cross-flow*, perpendicular to the detector flow. Cross-flow drives the sample towards the channel "accumulation" wall. The diffusion continuously forces the molecules and particles away from the accumulation wall until the equilibrium between cross-flow and diffusion is reached, resulting in a different displacement of molecules and particles according to differences in hydrodynamic radii. The higher the sample's diffusion coefficient, the greater the mean distance from the accumulation wall, and therefore it results in a higher velocity along the channel axis when the *detector flow* is applied. The sample (with a size smaller than approximately 1 μm) elutes in order of increasing hydrodynamic radius, which is called *normal elution* mode. Separation of particles with size larger than 1 μm is carried out in the opposite elution order, and it is called *steric elution* [24]. Knowing the properties of the channel (such as channel thickness, detector, and cross-flow rates), we can calculate the diffusion coefficient and the hydrodynamic radius based on the retention time in A4F technique.

Unlike the techniques mentioned above, AF4 has no stationary phase/packing material, which minimizes the sample-stationary phase interaction and shear degradation of the sample. AF4 has a wide separation range in size from 1 nm up to micrometers and it is compatible with a variety of solvents [9, 12]. In addition to separation and characterization, another advantage is the ability to analyze complex samples under conditions close to native ones, including appropriate buffers of a given ionic strength [25]. Individual eluates of the sample can be collected in narrow fractions for additional "offline" analysis using other methods, including electron microscopy for morphological analysis and SDS-PAGE/Western blot for the confirmation of purity and identity of individual separated proteins.

In this study, we used AF4 equipped with UV-DAD/MALS/DLS detectors for analysis and complex characterization of the recombinant pentameric protein as a promising antigen for construction and industrial production of an anti-circovirus vaccine for pigs.

Materials and methods

Insertion of sequences of the capsid protein of porcine circovirus 2b (PCV2b) into universal baculovirus transfer vectors

For pentamer VP1-Cap, the entire PCV2b Cap sequence was amplified using PCR primers introducing BamHI sites to the 5′ end and a His-tag (6 x His) and KpnI to the 3′ end; the sequence was cloned into the pFastBac1-VP1 vector cleaved by BamHI and KpnI. The resulting transfer vectors were termed pFastBac1-VP1-Cap-His. Vectors based on pFastBacI were used to prepare recombinant baculoviruses. The molecular weight of the pentameric VP1-Cap-HIS protein is 356 kDa; monomer fusion protein has a molecular weight of 71 kDa, where VP1 has 45 kDa [8].

Recombinant baculovirus preparation

Recombinant baculoviruses were produced according to the manufacturer's instructions (ThermoFisher Scientific, Bac-to-Bac system). Briefly, *E. coli* DH10Bac containing a bacmid and helper vector were transformed using individual transfer vectors. Recombinant bacmid DNA from positive bacterial colonies was isolated (ThermoFisher Scientific, PureLink™ HiPure Plasmid DNA Miniprep Kit) and verified by PCR. Sf9 insect cells were transfected with bacmid DNA using lipofection (ThermoFisher Scientific, Celfectin II reagent). Sf9 cells (Gibco) were grown in suspension culture at 27.5 °C in SFM900II medium (Gibco) in New Brunswick temperature-controlled shaker. Recombinant baculoviruses released into the growth media (V_0) were harvested 72 h after transfection and used for further multiplications by infection of insect cells to generate high-titer viral stocks [8].

Generation of high-titer viral stocks and protein production in insect cells

Baculoviruses were generated from recombinant bacmids according to the guidelines of the Bac-to-Bac protocol. To amplify the virus, $3.5{\cdot}10^7$ cells in 10 ml of SFM900II medium supplemented with 1.5% FBS were infected with V_0 at a multiplicity of infection (MOI) = 0.1 in 50 ml TPP® TubeSpin bioreactor with rotation speed 200 rpm. After 4 days, the supernatant (V_1) was collected, and another $3.5{\cdot}10^7$ cells in 10 ml SFM900II medium supplemented with 1.5% FBS were infected with V_1 at MOI = 5. Four days after incubation at 27.5 °C and 200 rpm, the supernatant (V_2) was collected. Two milliliters of V_2 at MOI = 5 was used to infect $9{\cdot}10^8$ cells in 300 ml of SFM900II medium in 600 ml TPP® TubeSpin bioreactor bottles at 140 rpm for protein production over 48 h.

Nuclear extract (NE) preparation

Baculovirus-infected cells were harvested by centrifugation at 2000*g* for 10 min; the cell pellet was resuspended in 40 ml ice-cold lysis buffer (137 mM NaCl, 10 mM Na_2HPO_4, and 1.8 mM KH_2PO_4) and allowed to swell on ice for 20 min with intermittent mixing. Centrifugation at 4000*g* and 4 °C for 10 min was used to separate the supernatant (CE1) and nuclei. The pellets with nuclei were washed twice with 10 ml of ice-cold lysis buffer, and the supernatant was collected (CE2, CE3) by centrifugation at 4000*g* and 4 °C for 10 min. The pellets with nuclei were redissolved in 10 ml of ice-cold NE buffer (20 mM HEPES 7.5 pH, 400 mM NaCl, 2 mM EDTA, and 1 mM DTT) and incubated on ice for 30 min. The supernatant (NE) was collected by centrifugation at 4000*g* and 4 °C for 10 min. Nuclear extract was centrifuged at 210,000*g* (rotor SW 41 Ti) for 2 h at 10 °C and the pellet was resuspended in PBS and stored at 4 °C for further analysis.

SDS protein electrophoresis (SDS-PAGE) and Western blot analysis

Concentrated (Pierce™ Protein concentrator PES) protein fractions (for concentration results, see Supplementary Information (ESM)) were boiled in Laemmli sample buffer for 5 min and resolved in 12.5% (fractions) and 10% (primary sample) SDS-polyacrylamide gel. Separated proteins were stained with Coomassie blue (Sigma-Aldrich). For Western blot analysis, proteins were electro-transferred onto a nitrocellulose membrane (Serva) in blotting buffer (0.3% Tris, 1.44% glycine, 20% methanol) at 15 V for 45 min. The membrane was incubated with 5% skim milk in Tris-buffered saline containing 0.05% Tween-20 (TBS-T) for 1 h, then stained with Anti-6X His tag HRP antibody (ab1187, ABCAM) for 1 h. The membrane was washed (3 × 10 min) in TBS-T after each incubation. The membranes were developed using the Pierce ECL Western Blotting Substrate reagent (ThermoFisher Scientific) and analyzed with Azure Biosystems C300 (Azure Biosystems, Inc.) and cSeries Capture Software.

MADLS measurement

The suspensions were measured using low-volume quartz batch cuvette, ZEN2112 (Malvern Panalytical Ltd, UK), at the constant temperature of 25 °C, and using temperature ramp in a range from 20 to 65 °C with the step of 5 °C for stability measurements. Multi-Angle Dynamic Light Scattering measurements (MADLS®) were performed with a Zetasizer Ultra instrument (Malvern Panalytical Ltd, UK). The instrument was equipped with a 633-nm HeNe laser and had detection angles at 173°, 90°, and 13°, respectively. The size distribution, z-average diameter, polydispersity index (PDI), and particle concentration (particles/ml) were obtained using ZS Xplorer software (Malvern Panalytical Ltd, UK).

Transmission electron microscopy

The suspension after fractionation was covered with a grid coated with Formvar film (Sigma-Aldrich, Czech Republic) and carbon (Agar Scientific, Austria). The grid was removed from the suspension after 1 min, and the residual water was dried with a strip of filtration paper. A drop of 2% aqueous-phospho-tungstic acid was placed onto the grid for a few seconds, and then, the excess stain was dried with filtration paper. Samples were observed under an electron microscope Philips 208 S Morgagni (FEI, Czech Republic) at ×7500 magnification and an accelerating voltage of 80 kV.

Immunogold labelling Labelling was performed according to the protocol [26]. Different suspensions of the pentameters were incubated with native primary antibodies PCV2Cap H9 (Exbio, Prague, Czech Republic) for 1 h at 60 °C and kept at

4 °C overnight. Then, the suspension was incubated for 1 h at room temperature with gold particles conjugated with protein A (Sigma-Aldrich, GE). The immunogold-labelled pentamers were prepared for negative staining as described previously and observed under a transmission electron microscope.

AF4 separation and analysis

The Eclipse separation system (Eclipse AF4, Wyatt Technology Europe GmbH, Germany) was connected to an isocratic pump, degasser, and autosampler with a temperature control unit (Agilent 1260 Infinity II, Agilent Technologies, Germany). The Short separation channel (SC with the channel length of 18 cm) was equipped with a trapezoidal wide polyethylene terephthalate spacer (Wyatt Technology Europe GmbH, Germany) with 350-μm thickness (MW 350) and regenerated cellulose membrane (cutoff 10 kDa). The actual thickness of the channel (293 μm) was determined using channel-high correlation function based on elution of bovine albumin. For correlation, the Scout DPS software version 2.0.0.9 (Wyatt Technology Europe GmbH, Germany) was used. The separation system was connected to the UV-VIS detector (Agilent 1260 Infinity II, Agilent Technologies) and MALS detector DAWN HELEOS II (Wyatt Technology Europe GmbH, Germany) equipped with a GaAs 658-nm laser and, using 18 angular positions (between 15 and 160°), with DLS detector at the angle of 149°. Filtered (0.1 μm) and preserved (0.04% ProClin™ 300, Sigma-Aldrich) Tris buffer (Tris 50 mM and NaCl 150 mM) pH 7.4 was used as the carrier liquid. The separation was performed at a constant temperature of 25 °C (Thermos$^{[PRO]}$ Wyatt Technology Europe GmbH, Germany). The samples were separated under the following conditions: The *detector flow* rate was kept constant at 1.0 ml/min; 50 μl of the sample was injected into the channel at a *cross-flow* rate of 1.5 ml/min for 3 min in the *focus-inject* mode (*inject flow* rate 0.2 ml/min) and further focused for 5 min at the same *cross-flow* rate. The elution profile was divided into three different categories: *constant* (Fig. 1a) *cross-flow* rate of 0.1, 0.25, and 0.5 ml/min for 60 min; *linear decreasing* (Fig. 1b) from the initial *cross-flow* rate of 2.0 ml/min decreasing to 0.0 ml/min over 40, 60, and 80 min; *exponential* (Fig. 1c) decreasing from the initial *cross-flow* rate of 2.0 ml/min to 0.0 ml/min over 60 min with a different slope of 10, 20, or 30. Based on these experiments, the *combined* (Fig. 1d) profile was created. The starting *cross-flow* rate of 2 ml/min with an exponential decrease to 0.25 ml/min over 20 min with the slope of 10 was followed by the constant *cross-flow* rate of 0.25 ml/min for 30 min. All elution profiles were extended by 10 min of elution and elution-inject profile with the *cross-flow* rate of 0.0 ml/min as a rinsing step.

The measurement was evaluated by the Astra software version 7.1.4.8 (Wyatt Technology Europe GmbH, Germany). The MALS detector (Wyatt Technology Europe GmbH, Germany) was calibrated with the HPLC grade toluene and normalized using isotropic scattered standard 1 mg/ml BSA in Tris buffer. The UV detector (Agilent 1260 Infinity II, Agilent Technologies) was set up at a wavelength of 280 nm. It was used as a concentration source with the UV extinction coefficient of 0.6670 ml/(mg cm).

Chemicals

All other chemicals, unless otherwise specified, were purchased from Sigma (St. Louis, MO). Ultrapure water was obtained from the Milli-Q® Reference Water Purification System (Merck KGaA, Darmstadt, GE).

Results and discussion

The individual elution profiles were evaluated in the term of size similarity assessment obtained from online DLS and from simplified retention equation, together with conformation information and resolution parameter.

The simplified retention Eq. (1) was used under the assumption of the normal elution mode elution without steric effect [12]:

$$t_R = \frac{w^2 \pi \eta R_{H-ret.}}{kT} \ln\left(1 + \frac{\dot{V}_c}{\dot{V}}\right) \quad (1)$$

where t_R is the retention time, w is the channel thickness, η is the viscosity of the mobile phase, $R_{H\text{-ret.}}$ is the hydrodynamic radius obtained from retention equation, k is the Boltzmann's constant, T is the thermodynamic temperature, $\dot{V}$ is the channel laminar *detector flow* rate, and $\dot{V}_c$ is the *cross-flow* rate. With constant experimental parameters, the hydrodynamic radius can be determined directly from the retention time using Eclipse simulation program, Scout (Wyatt Technology Europe GmbH, Germany) [12]. During the process, the separation channel is divided into a high number of small volumes. Then, for each volume element, the flow vectors and diffusion of the sample are calculated, concerning the changing flow rates during the elution [27].

The retention time of the individual peaks together with the width $w_{1/2}$ measured at one-half of the given peak height (width of the peak for the polydisperse sample is not well defined) was used for determination of the modified resolution parameter R_s [28]:

$$R_S = \frac{t_{R2} - t_{R1}}{w_{1/2_2} + w_{1/2_1}} \quad (2)$$

The size of the particles was also expressed as the *hydrodynamic radius* (R_h) obtain by the Dynamic Light Scattering technique using the Stokes-Einstein equation. Assuming the sample is a compact sphere [29],

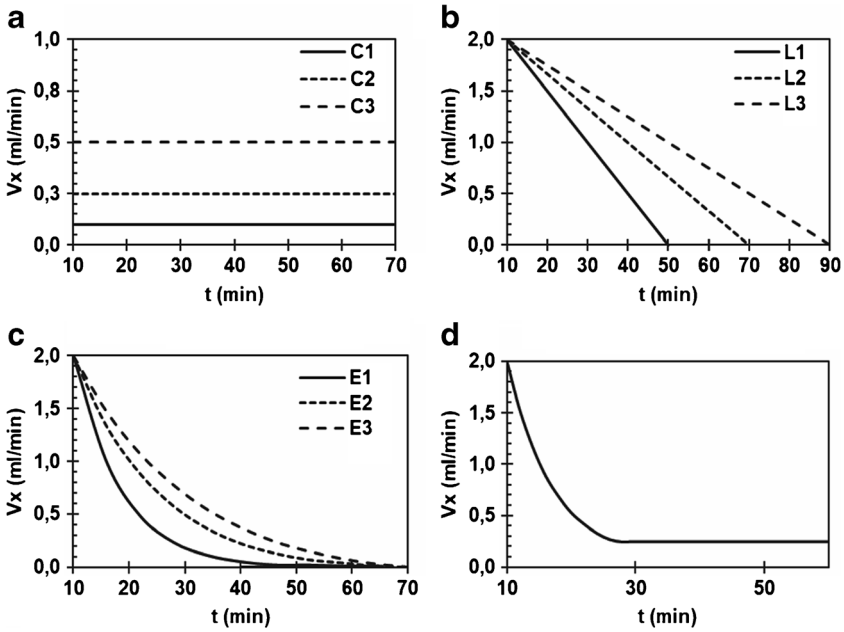

Fig. 1 Plots of different cross-flow profiles: **a** constant cross-flow profiles with the rate 0.1, 0.25, and 0.5 ml/min for C1, C2, and C3, respectively; **b** decreasing linear profiles with the slope − 0.05 (L1), − 0.033 (L2), and − 0.025 (L3); **c** exponential decreasing profiles with the slope $\tau_{1/2}$ 10, 20, and 30 for E1, E2, and E3, respectively; **d** final, combinative cross-flow profiles

$$R_h = \frac{kT}{6\pi\eta D} \tag{3}$$

The hydrodynamic radius is measured by a single-angle detector, 173° for batch DLS, and 143° for the flow cell detector [29]. The intensity and number of distributions are obtained from Multi-Angle Dynamic Light Scattering (MADLS) which delivers an angular-independent particle size distribution with increased resolution (typically from 3:1 for single-angle measurements) to 2:1 by combining the scattering information detected at three angles (173°, 90°, and 13°) [29, 30].

The R_g/R_h ratio (ratio of the radius of gyration R_g and the hydrodynamic radius R_h) can be used for determination of comformation of the eluting particles. The R_g was determined using multi-angle light scattering. The angular dependence of the intensity of the scattered light is evaluated using Berry formalism [12]:

$$\sqrt{\frac{Kc}{R_\theta}} = \frac{1}{\sqrt{MP(\theta)}} + A_2 c\sqrt{MP(\theta)} \tag{4}$$

where M is the molecular weight, $P(\theta)$ is the particle scattering function, A_2 is the second virial coefficient, c is the concentration, and K is the light scattering constant. The particle scattering function is approximated for small angles as:

$$\lim_{\theta\to 0} P(\theta) = 1 - \frac{16\pi^2 n_0^2}{3\lambda_0^2}\sin\left(\frac{\theta}{2}\right)\left\langle R_g^2\right\rangle \tag{5}$$

where λ_0 is a wavelength of the incident light in a solvent with a refractive index of n_0. The $\sqrt{Kc/R(\theta)}$ is plotted against $\sin^2(\theta/2)$, the abscissa is constructed, and, from the slope, the R_g is determined [12, 17]. Table 1 shows information about the sample conformation related to R_g/R_h ratio.

AF4 separation of pentameric protein particles using different cross-flow profiles

Separation parameters such as temperature and ionic strength of the carrier liquid were selected to preserve the native state of proteins and obtain high recoveries from samples. The thermal stability (for the DLS analysis, see ESM Fig. S1) shows no thermally induced aggregation up to 50 °C. The mobile phase composition and salt concentration were maintained in accordance with the protocol of the VP1-Cap preparation [8]. Additional data are presented in supporting information.

The adjustable cross-flow rate and elution profile are important separation factors affecting the resolution. They may cause unwanted sample-membrane interactions reducing sample recovery. In our study, different elution profiles were tested, including the constant, linear, and exponential decline of the cross-flow rate. Figure 2 shows three fractograms with different constant cross-flow rates. The size of the eluting species is expressed on the minor axis. The size is expressed as a hydrodynamic radius from online DLS detector. The hydrodynamic radius is

Table 1 The R_g/R_h ratio with the corresponding sample conformation. The theoretical lower value of the ratio suggests solid structures; the value increases with decreasing structure density [14]

R_g/R_h	Conformation
< 0.7	A highly expanded macromolecule or swollen microgel structure [14]
0.778	Hard sphere [31]
0.998	Soft sphere [32]
1.0–1.5	Branched molecule [33]
1.5–2.1	Random coil [34]
> 2	Rod-like structure [35]

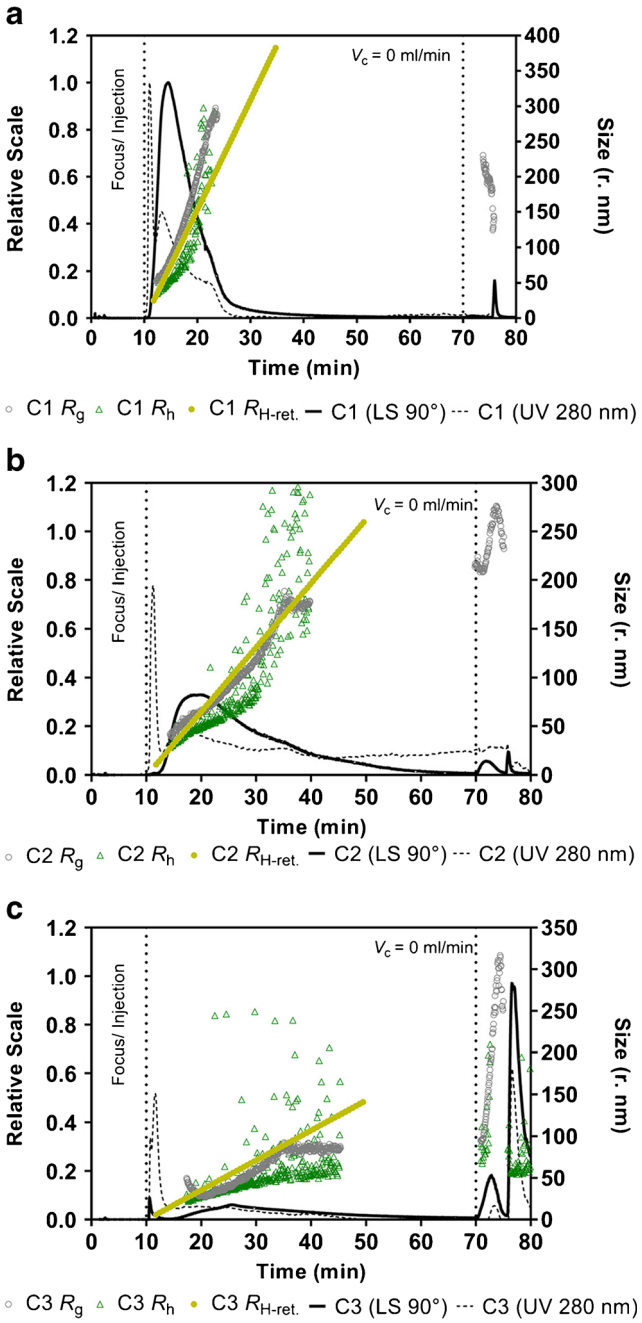

Fig. 2 Fractograms with different cross-flow rates of the constant cross-flow profiles: **a** 0.1 ml/min; **b** 0.25 ml/min; **c** 0.5 ml/min. The relative scale shows normalized data of the light scattering (90°, full line) and UV absorbance 280 nm (dashed line). The right axis represents the hydrodynamic radius based on online DLS measurement, hydrodynamic radius based on the retention equation calculation, and the radius of gyration based on the online MALS measurement. The $V_c = 0$ mil/min marks the time where the cross-flow rate decreases to 0

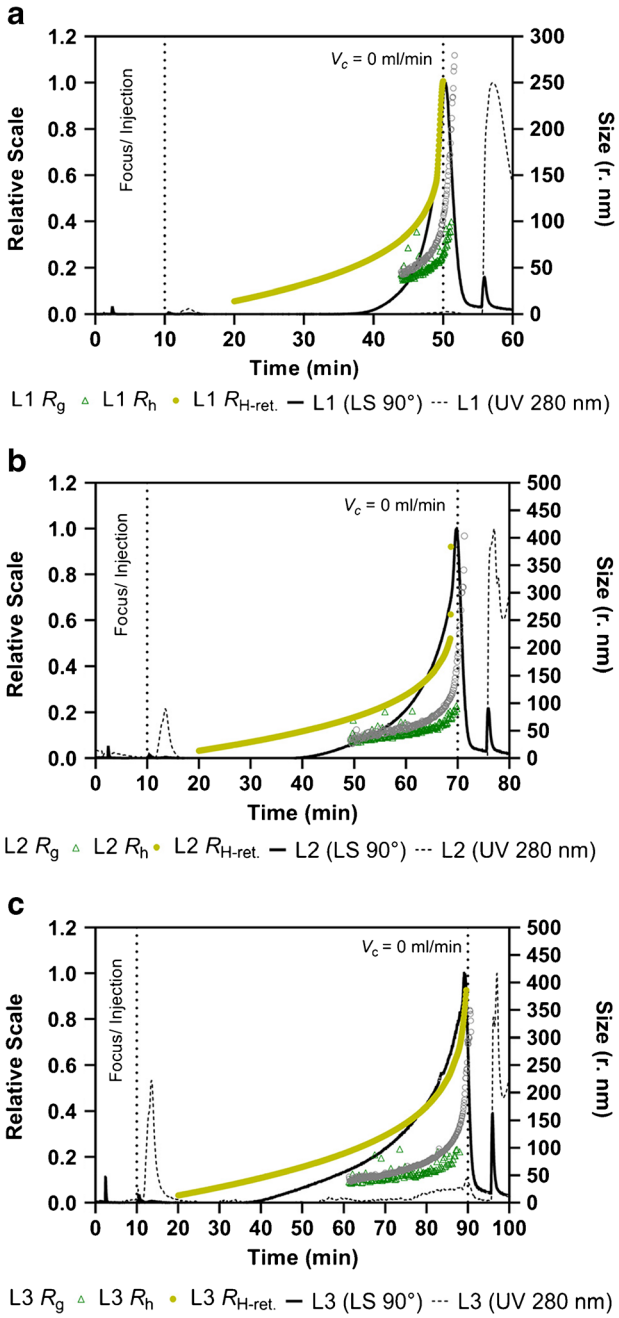

Fig. 3 Fractograms with different cross-flow rates, linearly decreasing from 2.0 to 0.0 ml/min with different slopes: **a** L1 40 min; **b** L2 60 min; **c** L3 80 min. The relative scale shows normalized data of the light scattering (90°, full line) and UV absorbance 280 nm (dashed line). The right axis represents the hydrodynamic radius based on online DLS measurement, hydrodynamic radius based on the retention equation calculation, and the radius of gyration based on the online MALS measurement. The $V_c = 0$ mil/min marks the time where the cross-flow rate decreases to 0

calculated from the simplified retention equation and the gyration radius R_g from online MALS detector. In general, the elution starts at the 10th minute of the fractogram (after the injection and the focusing step). Immediately after switching to elution mode, we can observe elution of species with a strong UV absorbance and a small light scattering signal, which are impurities of proteins with small molar masses. The resolution between UV peak and the peak of the light scattering signal from pentameric particles is increasing with higher cross-flow rates.

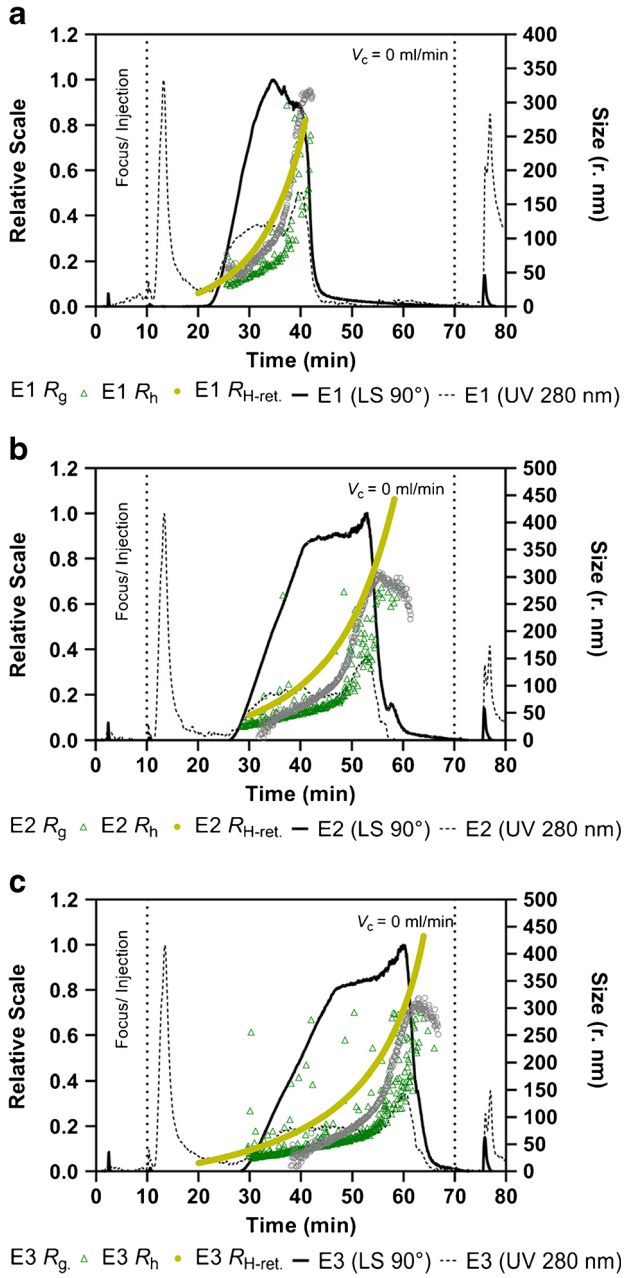

Fig. 4 Fractograms with different cross-flow rates, exponential decreasing from 2.0 to 0.0 ml/min over 60 min with different slopes: **a** E1 10; **b** E2 20; **c** E3 30. The relative scale shows normalized data of the light scattering (90°, full line) and UV absorbance 280 nm (dashed line). The right axis represents the hydrodynamic radius based on online DLS measurement, hydrodynamic radius based on the retention equation calculation, and the radius of gyration based on the online MALS measurement. The $V_c = 0$ mil/min marks the time where the cross-flow rate decreases to 0

For the cross-flow rate of 0.1 ml/min (Fig. 2a), pentameric particles are co-eluting with protein impurities, which elute between 10 and 12 min. The hydrodynamic radius starts at 35 nm and grows linearly to 80 nm (17th minute of elution). Then, the hydrodynamic radius becomes scattered due to the presence of aggregates and low intensity of the scattered light. The hydrodynamic radius (based on retention equation $R_{H\text{-ret.}}$) starts at 28 nm and rises to 100 nm at the same elution time, which correlates with the measured hydrodynamic radius. The similarity between the hydrodynamic radius obtained from retention equation and measured by online DLS indicates that the sample is eluting according to the FFF separation mechanism and that there are no interactions between the sample and membrane (the relative difference between R_h and $R_{H\text{-ret.}}$ (ΔR) was below 10% for the individual, early eluting populations, ESM Fig. S3). The presence of the aggregates in the main peak is confirmed by the radius of gyration which rapidly increases in the middle of the main peak from the gyration radius of 50 to 300 nm.

In the case of the constant cross-flow rate C2 0.25 ml/min (Fig. 2b), the resolution between the main peak (eluting between 10 and 12 min) and peak at the beginning of the elution is better (R_s C1 0.74; R_s C2 0.78, ESM Table S3) compared to the cross-flow rate of 0.1 ml/min. The hydrodynamic radius from the online DLS is relatively narrow, from 28 to 90 nm in the 30th minute of the elution, which is followed by a scattered signal from a larger component, the aggregates. The presence of the aggregates is shown by the radius of gyration growing linearly from 40 to 110 nm with a sharp rise up to 175 nm in the 30th minute of elution. The $R_{H\text{-ret.}}$ is ranging from 20 to 130 nm. The ΔR is below 5% for early eluting sample populations.

The deviation of the measured hydrodynamic radius from the calculated radius is significant, especially for later elution times (the ΔR was over 30%), due to the starting sample-membrane interaction. As the cross-flow rate increases, the $R_{H\text{-ret.}}$ deviate from the measured radius to a greater extent. Higher cross-flow rates can promote higher sample-membrane interaction; the sample remains closer to the accumulation wall for a longer time, which is responsible for the undesirable interaction that may be the cause of the delayed elution compared to AF4 theory. The interaction is particularly evident in the case of the constant cross-flow of 0.5 ml/min (Fig. 2c). The hydrodynamic radius from the online DLS varies from 30 to 65 nm with the main peak eluting from time 18 min to approximately 40 min. The $R_{H\text{-ret.}}$ radius goes from 25 up to 110 nm for the same elution time. A relatively large portion of the sample is eluting, during the flush phase of the elution. At the 70th minute of elution, the cross-flow rate reaches 0.0 ml/min.

Figure 3 shows three different linear cross-flow profiles starting at 2.0 ml/min and decreasing to 0.0 ml/min over 40-, 60-, and 80-min periods for L1 (Fig. 3a), L2 (Fig. 3b), and L3 (Fig. 3c), respectively. For L1, L2, and L3, the high resolution between the void peak (10th minute of the elution time) and the light scattering peak of the pentameric particles (40th to 90th minute of the elution time) is observed (R_s for L1 was 6.59; clear signal was not obtained for the second eluting peak for L2 and L3). The hydrodynamic radius is scattered and is in

the range of 43~93 nm for L1, 33~99 nm for L2, and 38~99 nm for profile L3 at the elution time of 43~51, 49~70, and 61~88 min, respectively. A larger portion of particles is released when the cross-flow rate decreased to 0.0 ml/min (after the release peak). The $R_{H\text{-ret.}}$ in the same elution range is 75~255 nm for L1, 71~270 nm for L2, and 92~285 nm for L3. With the decreasing slope of the cross-flow, the main peak becomes wider. The $R_{H\text{-ret.}}$ value indicates a higher sample-membrane interaction characterized by a longer elution time of smaller particles (the ΔR_t was over 50% for L1, L2, and L3 profiles, ESM Fig. S3). The radius of gyration results shows a narrow size distribution in the range from 50 to 100 nm which is rapidly sharping up to 250 nm for 0.0 ml/min of the cross-flow. The sharp increase in the radius of gyration is the result of co-eluting aggregates. After the cross-flow off ($V_c = 0$ min/min), we observe a strong UV signal from protein impurities (release peak) which are retained in the channel due to the high cross-flow of 2.0 ml/min at the beginning of the elution. The UV signal is negligible in the range of the elution of the main particles due to the low concentration of the sample in the elution peak and a possible scattering effect. The release peak is relatively high compared to the fractograms with other elution profiles.

Figure 4 shows fractograms with different exponential decreasing cross-flow profiles starting at 2.0 ml/min and decreasing to 0.0 ml/min over the 60 min with a different slope

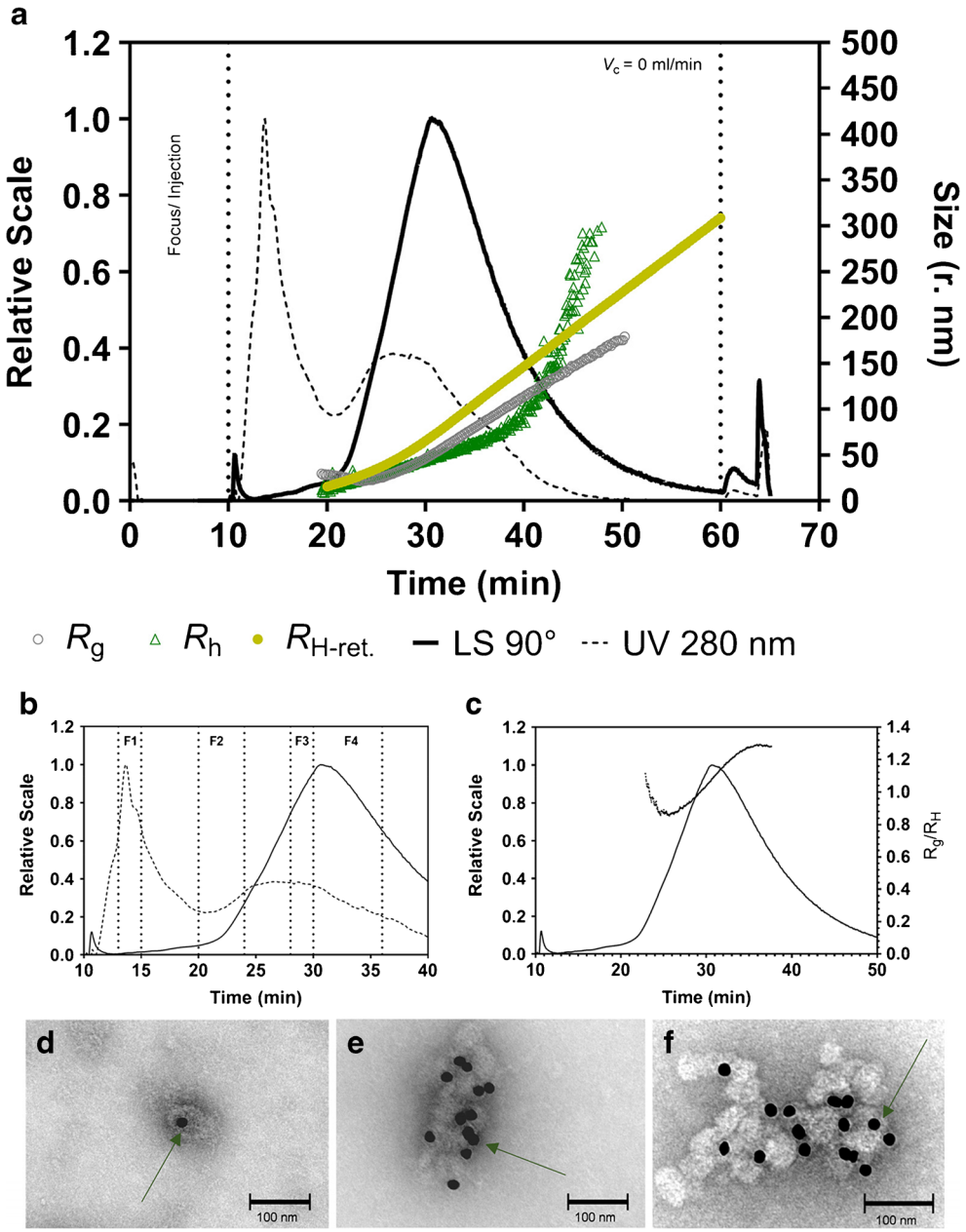

Fig. 5 **a** Fractogram of the elution profile combined with the cross-flow rate starting at 2 ml/min and decreasing to 0.25 ml/min over 20 min with the slope of 10 followed by a constant cross-flow of 0.25 ml/min over 30 min. The relative scale shows normalized data of the light scattering (90°, full line) and UV absorbance 280 nm (dashed line). On the right axis: hydrodynamic radius based on online DLS measurement; hydrodynamic radius based on the retention equation calculation; the radius of gyration based on the online MALS measurement. The $V_c = 0$ mil/min marks the time where the cross-flow rate decreases to 0. **b** Fractogram with differently marked fractions F1–F4. **c** A detail of the main peak with R_g/R_h on the right axis. **d**–**f** TEM images of the pentamers based on the individual fractions (**d**—F2, **e**—F3, and **f**—F4). Gold nanoparticles with H9 antibody selectively bound to the pentameric Cap protein are marked

of 10, 20, and 30 for E1 (Fig. 4a), E2 (Fig. 4b), and E3 (Fig. 4c), respectively. Exponential elution profiles have a narrow hydrodynamic radius distribution at the range of 33~70 nm (25~35 min) for E1, 28~85 nm (28~49 min) for E2, and 42~95 nm (29~55 min) for E3. The $R_{H\text{-ret.}}$ for the same elution range is 40~130 nm, 38~200 nm, and 35~210 nm concerning individual elution profiles. The ΔR for early eluting sample populations (individual pentamers) is decreasing with an increasing slope from approximately 15% for E1 to approximate 7% size difference for E3. The early eluting species of the pentameric protein particles correlates with the hydrodynamic radius (based on the retention equation). At later elution times, the LS data becomes scattered due to the co-eluting aggregates. For slopes 20 and 30, the hydrodynamic radius distribution is narrower. The effect of the higher cross-flow rates over an extended period increases the interaction of the sample and the membrane, resulting in longer sample retention in the channel and prolonged elution times. The radius of gyration shows us the presence of large aggregates at the end of the light scattering peak. The narrow range from 40 to 100 nm is followed by a rapid increase up to 300 nm. No significant light scattering signal was observed for the released peak (75th minute of the elution).

Based on our previous experiments with different elution profiles (Figs. 2, 3, and 4), the combinative elution profile was set up as follows: Cross-flow starts at the rate of 2 ml/min and exponential decreases to the rate of 0.25 ml/min over 20 min with the slope of 10. The exponential decrease is then followed by a constant cross-flow rate of 0.25 ml/min over 30 min. The resulting fractogram is shown in Fig. 5a. The protein impurities not related to recombinant pentameric VP1-Cap elute within the first 10 min of elution. The sharp UV peak is followed by elution of particles with the hydrodynamic radius starting at 15 nm ranging up to 100 nm. The $R_{H\text{-ret.}}$ is ranging from 20 up to 150 nm within the interval of the main peak (20–40 min of the elution). From the approximately 40th minute, the large aggregates with the radius ranging from 125 to approximately 300 nm start to elute. Light scattering data in this area are scattered due to the low concentration of aggregates. By measuring the radius of gyration, we can distinguish individual units of the pentameric particles. Pentameric particles start to be eluted in the approximately 20th minute of the run, the starting R_g is relatively constant and fluctuates around 25 ± 2 nm. Around the 25th minute, we can observe a sudden R_g increase with elution of super-unit pentameric structures with R_g ranging from 30 to 80 nm. The aggregates eluted at 40th minute range from 110 to 180 nm. Figure 5c shows a detail of the main peak of the R_g to R_h ratio (conformation plot). For individual pentameric units, the ratio is in the range of 0.8 to approximately 1. The range value is convenient for the soft sphere conformation [32]. The R_g/R_h ratio gradually increases with the elution of the super-unit pentameric structures up to the value of 1.3, which corresponds to the branched structure [33] of randomly associated pentamers. The obtained values and structures are in good agreement with structures obtained by transmission electron microscopy (Fig. 5d, e, f) where the individual pentameric particles have the longest axis of about 12 nm. The R_g/R_h ratio drops sharply after about 40 min of elution. The drop is due to a sudden increase in the value of the hydrodynamic radius. The ratio does not reflect the overall character of the sample but only reflects the scattered DLS signal of low concentrated aggregates. The calculated values of $R_{H\text{-ret.}}$ correspond to the measured values, especially for small, individual pentameric particles (the ΔR is below 4%). As the size of the eluting particles increases, the measured and calculated values deviate (ΔR up to 30%). The deviation is lower in the combined elution profile compared to the individual elution profiles. The cause of this deviation may be in the structure of individual self-associates of pentamers. The offline DLS analysis of the primary sample demonstrated the presence of individual pentamers as well as the existence of self-associates, and larger aggregates (Fig. 6a and b). According to the R_g/R_h ratio measurement (value >1.3) and TEM analysis (Fig. 5d and e), the self-associates of pentameric structures have a branched structure [33]. However, the calculated hydrodynamic radius is approximation on spherical particles, and only the individual pentameric protein particles meet the definition of a spherical particle (the spherical particles appear on EM analysis and R_g/R_h with a value of 0.8 correspondings to a soft sphere [32]). By comparing the DLS measurement of the primary sample with the individual fractions (Table 2), we could state that during AF4 separation, no further agglomerates are formed.

Table 2 Summary table of MADLS measurement

	Concentration (particles/ml)			z-average (d. nm)	PDI
	Peak one	Peak two	Peak three		
Primary sample	$2.97\pm0.92\cdot10^{13}$	$1.87\pm0.43\cdot10^{11}$	$6.34\pm0.88\cdot10^{09}$	127±1	0.265±0.006
F2	$4.25\pm1.92\cdot10^{11}$			38±2	0.301±0.051
F3	$2.00\pm0.13\cdot10^{10}$			64±2	0.159±0.009
F4	$3.53\pm0.02\cdot10^{09}$			97±3	0.192±0.048

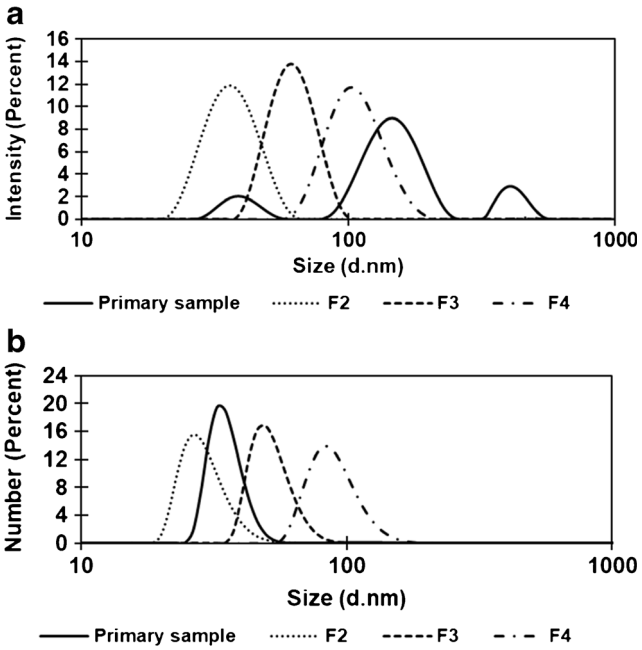

Fig. 6 MADLS analysis of primary sample (sample before A4F purification) and fractions F2–F4. **a** The distributions by the intensity. **b** The distributions by the number

Batch analysis

Different fractions were collected based on the fractogram (Fig. 5b) and subjected to further offline analysis. Figure 6a shows the intensity and Fig. 6b the number distribution of the MADLS measurement. The full black line represents the sample before fractionation (primary sample). The intensity distribution consists of three peaks with the first having maximum at 38 nm corresponding with the size of the single pentameric unit, the second peak with a maximum at 150 nm corresponding to the super-unit pentameric structures, and the third peak corresponding to larger aggregates with a diameter of approximately 400 nm. The light scattering signal from the first fraction was not sufficient for batch DLS analysis; the results are not included. Fraction 2 (F2) shows a maximum at 37 nm, which corresponds to the first peak of the primary sample. With the increasing elution time, the diameter is increasing to 65 nm and 105 nm for F3 and F4, respectively. The number distribution of the primary sample (Fig. 6b) shows that the majority of the particles have a diameter of about 38 nm. This corresponds to the concentration measurement presented in Table 2 where the concentration increases with individual peaks of $2.97 \cdot 10^{13}$; $1.87 \cdot 10^{11}$; and $6.34 \cdot 10^{09}$ particles/ml for the first, second, and third populations, respectively.

Fraction F2 consists mainly of small individual pentameric protein units with z-average 38 nm and a concentration of $4.25 \cdot 10^{11}$ particles/ml. Fraction F3 with a larger population (z-average of 64 nm) contains $2.00 \cdot 10^{10}$ particles/ml, and F4 (z-average 97 nm) with the concentration of $3.59 \cdot 10^{9}$ particles/ml corresponding to the large, super-units of the pentamers. The sample recovery was calculated based on the comparison of the area under the UV curve from the elution without the use of the cross-flow (Flow-thru) with the individual fractions. For the calculated area and mass, see supporting information (ESM Table S2). The percentage mass recovery for F1 is 66%; for fractions F2–F4, the mass recovery was 48%. The Flow-thru peak starts elution immediately upon injection, without excessive tailing (see ESM Fig. S2). The Flow-thru peak profile together with the mass recovery of about 116% indicates no sample-membrane interaction.

The polydispersity index (PDI) in the primary sample is 0.265, indicating low polydispersity; however, the value is affected by the presence of three populations, which, like z-average value, in a sample with multiple populations, do not fully reflect the nature of the analyte. The polydispersity in an individual fraction is 0.301 for F2, 0.159 for F3, and 0.192 for F4. Low polydispersity values indicate that no larger particles co-elute within the different fractions, especially in the fractions F3 and F4.

The analysis of individual TEM fractions shows both the structure of the individual pentamers corresponding to the R_g/R_h values and the preserved native nature of the protein pentameric particles. Gold nanoparticles with H9 antibody selectively bind to the pentameric Cap protein only in the native state in fractions F2, F3, and F4 (Fig. 5d, e, f respectively). SDS-PAGE and Western blot analyses were performed on the concentrated fractions and primary sample (Fig. 7). By selective staining for His-tag group by Anti-6X His, the purity of the individual fractions was demonstrated. In fraction F1, the band at 70 kDa (band corresponding to denatured pentameric protein particles) is not visible.

Conversely, low molecular weight proteins are present, whose early elution time at given cross-flow corresponds to the AF4 theory. The visible band is especially present in fractions F3 and F4. Fraction F2 containing the largest number of particles (Table 2) does not show such a proportion of individual His-Tag groups. The band disproportion is caused by the structure of larger clusters of pentameric protein particles where the size expressed as z-average (Table 2) in F3 is about twice the fraction of F2 (z-average of F3 is 64 nm, and F2 is 38 nm). However, the volume of the particles, whose size will vary twice, will be eight times greater. Thus, larger particles, specifically particles in fractions F3 and F4, have a much greater His Tag group density than the fraction F2 as seen in Fig. 7a and b. Figure 7b also shows pentameric doublet in fractions F3 and F4, a band of about 140 kDa, resulting from the conjugation of individual proteins during denaturation.

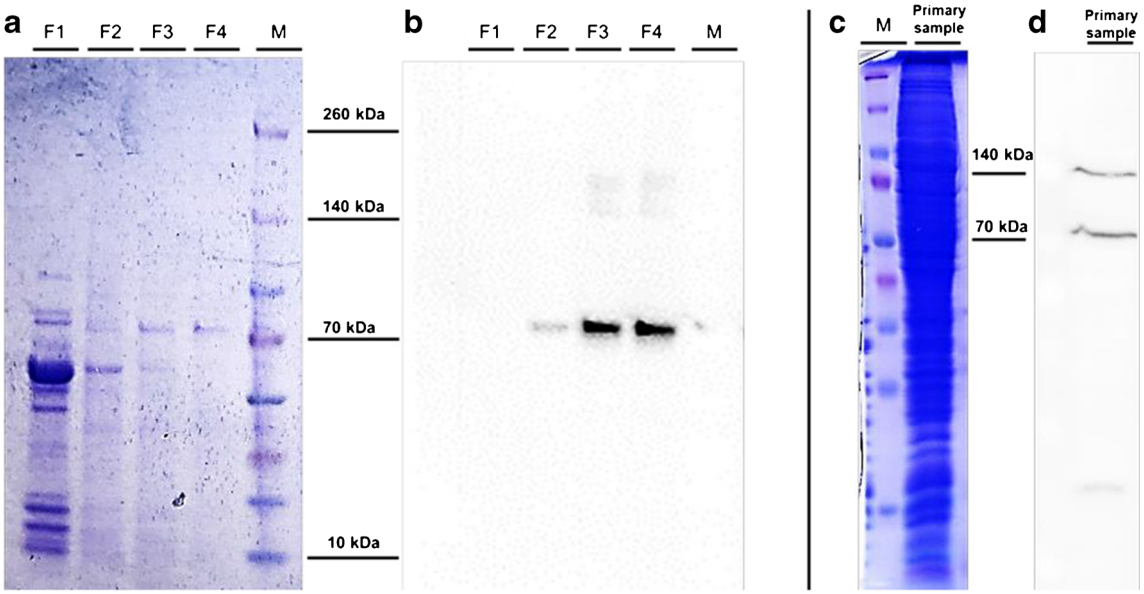

Fig. 7 The sodium dodecyl sulphate–polyacrylamide gel (12.5% for **a** and 10% for **c**) electrophoresis (SDS-PAGE) stained with the Coomassie blue dye: **a** individual fractions (F1–F4); **c** primary sample before fractionation. Western blot analysis; **b** individual fractions (F1–F4); **d** primary sample. M stands for markers of protein standards

Conclusions

Asymmetric flow field-flow fractionation system with UV, MALS, and online DLS detection was used for separation and characterization of pentameric protein particles and their aggregates. Different elution profiles were tested to determine the optimal separation conditions. The exponential decrease in combination with the constant cross-flow profile was found to be most suitable for optimal separation because of reducing overall separation time while maintaining separation efficiency. Individual fractions were further subjected to offline DLS, TEM, and SDS-PAGE analyses. The overall purity and quality of the individual fractions were assessed by SDS-PAGE/Western blot analysis. The measured particle size, expressed as the hydrodynamic radius, corresponds to the hydrodynamic radius values obtained from the simplified retention equation, in particular for the elution of individual protein pentamers. The data suggests that the deviation is due to the structure of larger pentameric multicomplexes and minimal sample and membrane interactions. The values of R_g/R_h ratios corresponded to the structures visualized by offline TEM analysis in each fraction. By comparison of the offline DLS measurement of the primary sample and the fractions, we showed that no additional aggregates are generated due to AF4 separation. The immunogold labelling of individual fractions together with SDS-PAGE/Western blot analysis showed preservation of the native structure of the pentameric antigen. Thus, AF4 working under native conditions proved itself to be a technique suitable for the separation and analysis of the large recombinant protein complex composed of a carrier that forms the pentamer of a mouse polyomavirus VP1 capsid protein to which the porcine circovirus 2 capsid protein molecules are covalently attached. Therefore, the FFF method is also applicable as a part of rapid quality control analyses during biotechnological production of vaccines based on large recombinant antigens.

Supplementary Information The online version contains supplementary material available at https://doi.org/10.1007/s00216-021-03323-6.

Acknowledgements Access to instruments in the laboratory NanoPharm (a joint project of the Veterinary Research Institute and International Clinical Research Center (FNUSA-ICRC) (JT) is acknowledged, as well as support by the Education and Research Centre VRI-Malvern (JT, SM) and Education and Research Centre VRI-Wyatt (JT, DR).

Funding CEREBIT (Centre for Recombinant Biotechnology and Immunotherapy) CZ.02.1.01/0.0/0.0/16_025/0007397 (MR, JT); "FIT" (Pharmacology, Immunotherapy, nanoToxicology) CZ.02.1.01/0.0/0.0/15_003/0000495 (JT, MR); SOLID21 (project no. CZ.02.1.01/0.0/0.0/16_019/0000760) (JT).

Declarations

Conflict of interest The authors declare no competing interests.

Ethics approval Not applicable

Consent to participate Not applicable

Consent for publication All listed co-authors and institutions agreed with the submission of this paper.

References

1. Gillespie J, Opriessnig T, Meng XJJ, Pelzer K, Buechner-Maxwell V. Porcine Circovirus type 2 and porcine Circovirus-associated disease. J Vet Intern Med. 2009;23:1151–63. https://doi.org/10.1111/j.1939-1676.2009.0389.x.
2. Tischer I, Gelderblom H, Vettermann W, Koch MA. A very small porcine virus with circular single-stranded DNA. Nature. 1982;295:64–6. https://doi.org/10.1038/295064a0.
3. Allan GM, Hassard LE, Clark EG, Todd D, McNeilly F, Haines DM, et al. Characterization of novel circovirus DNAs associated with wasting syndromes in pigs. J Gen Virol. 1998;79:2171–9. https://doi.org/10.1099/0022-1317-79-9-2171.
4. Segalés J, Allan GM, Domingo M. Porcine circovirus diseases. Anim Health Res Rev. 2005;6:119–42. https://doi.org/10.1079/AHR2005106.
5. Fachinger V, Bischoff R, Ben JS, Saalmüller A, Elbers K. The effect of vaccination against porcine circovirus type 2 in pigs suffering from porcine respiratory disease complex. Vaccine. 2008;26:1488–99. https://doi.org/10.1016/j.vaccine.2007.11.053.
6. Beach NM, Meng X-J. Efficacy and future prospects of commercially available and experimental vaccines against porcine circovirus type 2 (PCV2). Virus Res. 2012;164:33–42. https://doi.org/10.1016/j.virusres.2011.09.041.
7. Meng XJ (2013) Circoviridae. In: Fields virology: Sixth Edition. Wolters Kluwer Health Adis (ESP).
8. Fraiberk M, Hájková M, Krulová M, Kojzarová M, Drda Morávková A, Pšikal I, et al. Exploitation of stable nanostructures based on the mouse polyomavirus for development of a recombinant vaccine against porcine circovirus 2. PLoS One. 2017;12:e0184870. https://doi.org/10.1371/journal.pone.0184870.
9. Giddings JC. A new separation concept based on a coupling of concentration and flow nonuniformities. Sep Sci. 1966;1:123–5. https://doi.org/10.1080/01496396608049439.
10. Podzimek S, Machotova J, Snuparek J, Vecera M, Prokupek L. Characterization of molecular structure of acrylic copolymers prepared via emulsion polymerization using A4F-MALS technique. J Appl Polym Sci. 2014;131. https://doi.org/10.1002/app.40995.
11. Podzimek S, Machotova J, Zgoni H, Bohacik P, Snuparek J. Application of A4F-MALS for the characterization of polymers prepared by emulsion polymerization: comparison of the molecular structure of styrene-acrylate and methyl methacrylate-acrylate copolymers. Polym Plast Technol Eng. 2016;55:1365–72. https://doi.org/10.1080/03602559.2016.1146957.
12. Podzimek S. Light scattering, size exclusion chromatography and asymmetric flow field flow fractionation. Hoboken: John Wiley & Sons, Inc.; 2011.
13. Wahlund KG, Giddings JC, Wahlund K-G, Giddings JC, Wahlund KG, Giddings JC, et al. Properties of an asymmetrical flow field-flow fractionation channel having one permeable wall. Anal Chem. 1987;59:1332–9. https://doi.org/10.1021/ac00136a016.
14. Guo P, Li Y, An J, Shen S, Dou H. Study on structure-function of starch by asymmetrical flow field-flow fractionation coupled with multiple detectors: a review. Carbohydr Polym. 2019;226.
15. Zhang H, Lyden D. Asymmetric-flow field-flow fractionation technology for exomere and small extracellular vesicle separation and characterization. Nat Protoc. 2019;14:1027–53. https://doi.org/10.1038/s41596-019-0126-x.
16. Hupfeld S, Ausbacher D, Brandl M. Asymmetric flow field-flow fractionation of liposomes: optimization of fractionation variables. J Sep Sci. 2009;32:1465–70. https://doi.org/10.1002/jssc.200800626.
17. Hupfeld S, Moen HH, Ausbacher D, Haas H, Brandl M. Liposome fractionation and size analysis by asymmetrical flow field-flow fractionation/multi-angle light scattering: influence of ionic strength and osmotic pressure of the carrier liquid. Chem Phys Lipids. 2010;163:141–7. https://doi.org/10.1016/j.chemphyslip.2009.10.009.
18. Eskelin K, Lampi M, Meier F, Moldenhauer E, Bamford DH, Oksanen HM. Asymmetric flow field flow fractionation methods for virus purification. J Chromatogr A. 2016;1469:108–19. https://doi.org/10.1016/j.chroma.2016.09.055.
19. Bousse T, Shore DA, Goldsmith CS, Hossain MJ, Jang Y, Davis CT, et al. Quantitation of influenza virus using field flow fractionation and multi-angle light scattering for quantifying influenza A particles. J Virol Methods. 2013;193:589–96. https://doi.org/10.1016/j.jviromet.2013.07.026.
20. Zhang X, Li Y, Shen S, Lee S, Dou H. Field-flow fractionation: a gentle separation and characterization technique in biomedicine. TrAC - Trends Anal Chem. 2018;108:231–8. https://doi.org/10.1016/j.trac.2018.09.005.
21. Qureshi RN, Kok WT. Application of flow field-flow fractionation for the characterization of macromolecules of biological interest: a review. Anal Bioanal Chem. 2011;399:1401–11.
22. Fraunhofer W, Winter G. The use of asymmetrical flow field-flow fractionation in pharmaceutics and biopharmaceutics. Eur J Pharm Biopharm. 2004;58:369–83. https://doi.org/10.1016/j.ejpb.2004.03.034.
23. Lampi M, Oksanen HM, Meier F, Moldenhauer E, Poranen MM, Bamford DH, et al. Asymmetrical flow field-flow fractionation in purification of an enveloped bacteriophage ϕ6. J Chromatogr B Anal Technol Biomed Life Sci. 2018;1095:251–7. https://doi.org/10.1016/j.jchromb.2018.07.008.
24. Moon MH. Flow field-flow fractionation: recent applications for lipidomic and proteomic analysis. TrAC - Trends Anal Chem. 2019;118:19–28. https://doi.org/10.1016/j.trac.2019.05.024.
25. Dou H, Li Y, Choi J, Huo S, Ding L, Shen S, et al. Asymmetrical flow field-flow fractionation coupled with multiple detections: a complementary approach in the characterization of egg yolk plasma. J Chromatogr A. 2016;1465:165–74. https://doi.org/10.1016/j.chroma.2016.08.062.
26. Gulati NM, Torian U, Gallagher JR, Harris AK. Immunoelectron microscopy of viral antigens. Curr Protoc Microbiol. 2019;53. https://doi.org/10.1002/cpmc.86.
27. Johann CD, Kaltenborn A, Schuch HD, Schumacher M. Method for optimizing the separation method for a given sample system by asymmetric field flow fractionation: DE102007047695A1. 2017.
28. Dou H, Lee YJ, Jung EC, Lee BC, Lee S. Study on steric transition in asymmetrical flow field-flow fractionation and application to characterization of high-energy material. J Chromatogr A. 2013;1304:211–9. https://doi.org/10.1016/j.chroma.2013.06.051.
29. Hiemenz PC, Rajagopalan R. Principles of colloid and surface chemistry. Boca Raton: CRC Press, Taylor & Francis Group; 1997. p. 33487–2742.
30. Cummins PG, Staples EJ. Particle size distributions determined by a "multiangle" analysis of photon correlation spectroscopy data. Langmuir. 1987;3:1109–13. https://doi.org/10.1021/la00078a040.
31. Brewer AK, Striegel AM. Characterizing the size, shape, and compactness of a polydisperse prolate ellipsoidal particle via quadruple-detector hydrodynamic chromatography. Analyst. 2011;136:515–9. https://doi.org/10.1039/c0an00738b.
32. Brewer AK, Striegel AM. Particle size characterization by quadruple-detector hydrodynamic chromatography. Anal Bioanal Chem. 2009;393:295–302. https://doi.org/10.1007/s00216-008-2319-y.

33. Zielke C, Stradner A, Nilsson L. Characterization of cereal β-glucan extracts: conformation and structural aspects. Food Hydrocoll. 2018;79:218–27. https://doi.org/10.1016/j.foodhyd.2017.12.036.
34. Runyon JR, Ulmius M, Nilsson L, Ray Runyon J, Ulmius M, Nilsson L, et al. A perspective on the characterization of colloids and macromolecules using asymmetrical flow field-flow fractionation. Colloids Surfaces A Physicochem Eng Asp. 2014;442:25–33. https://doi.org/10.1016/j.colsurfa.2013.04.010.
35. Coviello T, Kajiwara K, Burchard W, Dentini M, Crescenzi V. Solution properties of xanthan. 1. Dynamic and static light scattering from native and modified xanthans in dilute solutions. Macromolecules. 1986;19:2826–31. https://doi.org/10.1021/ma00165a027.